Microstructural characterization of ZrB$_2$–SiC based UHTC tested in the MESOX plasma facility

Davide Alfano [a], Luigi Scatteia [a], Frederic Monteverde [b], Eric Bêche [c], Marianne Balat-Pichelin [c,*]

[a] CIRA–Centro Italiano Ricerche Aerospaziali, Capua (CE) 81043, Italy
[b] CNR-ISTEC, National Research Council, Institute of Science and Technology for Ceramics, Faenza 48018, Italy
[c] PROMES-CNRS Laboratory, 7 rue du four solaire, Font-Romeu Odeillo 66120, France

Abstract

Microstructures were investigated for ZrB$_2$–SiC and ZrB$_2$–HfB$_2$–SiC ultra high temperature ceramics that were subjected to a high temperature plasma environment. Both materials were tested in the MESOX facility to determine the recombination coefficient for atomic oxygen up to 1750 °C in subsonic air plasma flow. Surfaces were analyzed before and after testing to gain a deeper insight of the surface catalytic properties of these materials. Microstructural analyses highlighted oxidation induced surface modification. Oxide layers were composed of silica with trace amounts of boron oxide and zirconia if the maximum temperature was lower than about 1550 °C and zirconia for higher temperatures. The differences in the oxide layer composition may account for the different catalytic behavior. In particular, the presence of a borosilicate glass layer on the surface of ZrB$_2$–SiC materials guarantees atomic oxygen recombination coefficients that are relatively lower than the coefficients measured when only zirconia is present. The oxidation processes of ZrB$_2$–HfB$_2$–SiC materials, associated with catalytic tests carried out up to 1550 °C, lead to the formation of hafnia as well as silica, and zirconia. The higher recombination coefficients measured in the case of ZrB$_2$–HfB$_2$–SiC materials can be correlated with the presence of hafnia which is probably characterized by higher catalytic activity compared to zirconia. In any case, the investigated materials demonstrate a low catalytic activity over the inspected temperature range with maximum values of recombination coefficients close to 0.1.

© 2010 Elsevier Ltd. All rights reserved.

Keywords: B. Electron microscopy; Surfaces; C. Chemical properties; D. Borides; Ultra high temperature ceramics

1. Introduction

Ceramic compounds based on metal borides, such as zirconium diboride (ZrB$_2$) and hafnium diboride (HfB$_2$) are usually defined as ultra high temperature ceramics (UHTCs) for their extremely high melting temperatures.[1,2] Of those UHTCs, ZrB$_2$ has a lower theoretical density (6.09 g/cm^3), which makes it an attractive base matrix for UHTC compounds aimed at aerospace applications such as sharp leading edges and hot structures on future generations of slender-shaped re-entry vehicles.[3–5] The thermally demanding trajectories foreseen for future spaceplane-like, winged re-entry vehicles dictates the need for base materials able to sustain operating temperatures approaching 2200 °C and to resist evaporation, erosion and oxidation in the harsh re-entry environment. These requirements stand well above the operational single-use tem-

perature limit of current TPS materials such as SiC-coated C-C composites.[6–10]

Transition metal diboride-based UHTCs are typically processed by hot pressing. Complex shaped components can then be obtained either using conventional diamond machining or electrical discharge machining (EDM), which is possible due to the electrical conductivity of the borides that is on the order of 10^6 S/cm.[11] Surface finish can be better controlled through conventional machining. Nevertheless, EDM is effective and can be used to machine UHTC pieces into complex shaped components like nose-cones or sharp leading edges.[12,13]

Despite having been studied for several decades, properties of UHTC materials such as emissivity and surface catalycity are still not known. A complete understanding of the radiative and catalytic behavior of UHTCs is pivotal for the specific application of hot structures, given the impact that these properties have on the final heat balance during re-entry. Such surface properties are strongly dependent on the surface modification that occurs during high temperature exposure. Therefore, a comprehensive understanding of the oxidation behavior and of the

Table 1
Some characteristics of the raw powders: specific surface area (s.s.a. obtained by BET method), particle size range (psr obtained by SEM) and main impurities.

	Company	Type	s.s.a. (m2/g)	psr (μm)	Main impurities[*] (wt %)
ZrB_2	H.C. Starck, Germany	grade B	1	0.2–10	O: 1; Hf: 0.2
HfB_2	Cerac, USA	325 mesh	–	0.5–5	Zr: 0.5
SiC	H.C. Starck, Germany	BF12	11.6	0.05–2	O: 1.65

[*] From suppliers.

related surface modification under relevant conditions is also crucial.

The objective of this paper is to report microstructural characterization of ZrB_2-SiC based UHTCs that were previously exposed to atomic oxygen flow in the MESOX – Moyen d'Essai Solaire d'OXydation – facility located in PROMES-CNRS for the measurement of the recombination coefficient. Within the MESOX experimental campaign, catalytic properties of two ZrB_2-SiC UHTC compositions were determined; more specifically, samples machined by diamond-loaded tooling (DLT) and samples machined by EDM were tested to assess the effect of the surface finish (different surface roughness, partial oxidation during machining) upon those properties.

2. Materials and experimental

2.1. Materials

Nearly full dense UHTC composites were obtained by hot-pressing of the following powder compositions (vol.%):

- Material A: ZrB_2 + 15 SiC
- Material B: ZrB_2 + 15 SiC + 10 HfB_2

with 2 (vol.%) $MoSi_2$ as a sintering aid.

ZrB_2 and β-SiC raw powders were from H.C. Starck, HfB_2 from Cerac Inc., and $MoSi_2$ from Sigma–Aldrich. Table 1 summarizes some characteristics of the raw powders used. The as-sintered materials A and B had bulk densities, evaluated using the Archimedes method (water as immersing medium), of 5.61 and 6.06 g/cm^3, respectively, which corresponds to relative densities of 99 and 98%. The powder mixtures were uniaxially hot-pressed in vacuum using an inductively heated graphite die, lined with a BN-sprayed graphitized sheet. Peak temperatures/dwell times/applied pressures were 1820 °C/15 min/30 MPa for material A, and 1900–1940 °C/45 min/40 MPa for material B, with an average heating rate of 20 °C/min. The temperature was measured by means of an optical pyrometer focused on the graphite die.

X-ray diffraction (XRD) investigations were performed by a Ni-filtered CuKα radiation X-ray diffractometer (model D500, Siemens, Karlsruhe, Germany). In the case of material A, the main identified phases were ZrB_2 and SiC. Instead, in material B, obvious changes in the starting composition took place during sintering. XRD analyses showed the formation of ZrB_2/HfB_2 solid solutions. Such solid solutions uphold the hexagonal structure of the main ZrB_2 phase, however the lat-

tice readily accommodates substitution of Hf atoms for Zr. The thermo-physical and mechanical properties of the two UHTC compositions have been extensively characterized in previous studies.[12,14]

The two sintered materials were cut and shaped into cylindrical billets 25 mm diameter and 2 mm thickness for catalycity measurements in the MESOX facility using either DLT or EDM.

In this study, the as-machined billets have been labeled as 'pristine' before high temperature exposure in the MESOX experiments. To distinguish between samples machined by EDM and DLT, the suffixes -EDM and -DLT were adopted.

2.2. Plasma exposure in MESOX

The catalycity measurements in the MESOX apparatus are described in details in previous papers.[15–18] In the current manuscript, only the test environment to which the UHTC samples were subjected during the determination of the recombination coefficient, γ, has been included.

The UHTC sample was put in a plasma reactor consisting of a silica tube (quartz), 50 cm length and 5 cm diameter with CaF_2

Table 2
Mean values of the atomic oxygen recombination coefficient of EDMed and DLTed ZrB_2-SiC specimens (material A). The uncertainty on the measured recombination coefficients is evaluated as ±30%.

EDM		DLT	
T (K)	Mean γ	T (K)	Mean γ
850–1200	0.008	1000	0.024
		1200	0.044
1400	0.016	1400	0.056
1600	0.017	1600	0.077
1800	0.019	1800	0.095
2000	0.029	–	–

Table 3
Mean values of the atomic oxygen recombination coefficient of EDMed and DLTed ZrB_2-HfB_2-SiC specimens (material B). The uncertainty on the measured recombination coefficients is evaluated as ±30%.

EDM		DLT	
T (K)	Mean γ	T (K)	Mean γ
1000	0.030	1000	0.016
1200	0.054	1200	0.040
1400	0.065	1400	0.069
1600	0.092	1600	0.105
1800	0.097	1800	0.115

viewports. The air plasma was generated by a 300 W microwave discharge surrounding the sample. A regulator, a gauge and a vacuum pump allowed for precise control of the total pressure during experiments. The airflow, coming from the top of the reactor and then pumped downward, was fixed at 4 l/h. The degree of dissociation of the air plasma was approximately 70% and the atomic oxygen density was approximately 10^{22} atoms/m^3 in these test conditions.[19] The sample was positioned 25 mm above the theoretical focus of the 6 kW solar furnace equipped with a variable opening shutter. With this shutter, the available incident concentrated solar flux can be controlled up to 5 MW m^{-2}. The concentrated solar energy had a Gaussian distribution on the sample surface.

At this position–25 mm above the focal point–solar flux and temperature were homogeneous over a region about 10 mm wide in the central zone of the sample. The temperature measurement was performed using a monochromatic optical pyrometer working at 5 μm taking into account the normal spectral emissivity at 5 μm previously measured at the PROMES-CNRS laboratory on these samples.[14]

Each sample was subjected to a step ramp in temperature from 600 °C to approximately 1750 °C at a total air pressure of 200 Pa. The recombination coefficient γ was measured every 200 °C with three measurements and three times at each temperature plateau. Each heating step lasted about 4 min including a 3 min isothermal hold for a total exposure time of about 60 min. In Tables 2 and 3 the mean values of the atomic oxygen recombination coefficient γ measured at different temperatures are listed for the two UHTC compositions.

2.3. Microstructure characterization

All specimens examined by Scanning Electron Microscopy (SEM, S-4500 Hitachi) were prepared using argon plasma sputtering with a gold target to obtain a 5 nm thick electrically conductive gold layer. Energy dispersive chemical analyses (EDS) were performed using a FEI XL30 FEG ESEM apparatus with EDAX X-ray detector on samples without any coating.

A-EDM

A-DLT
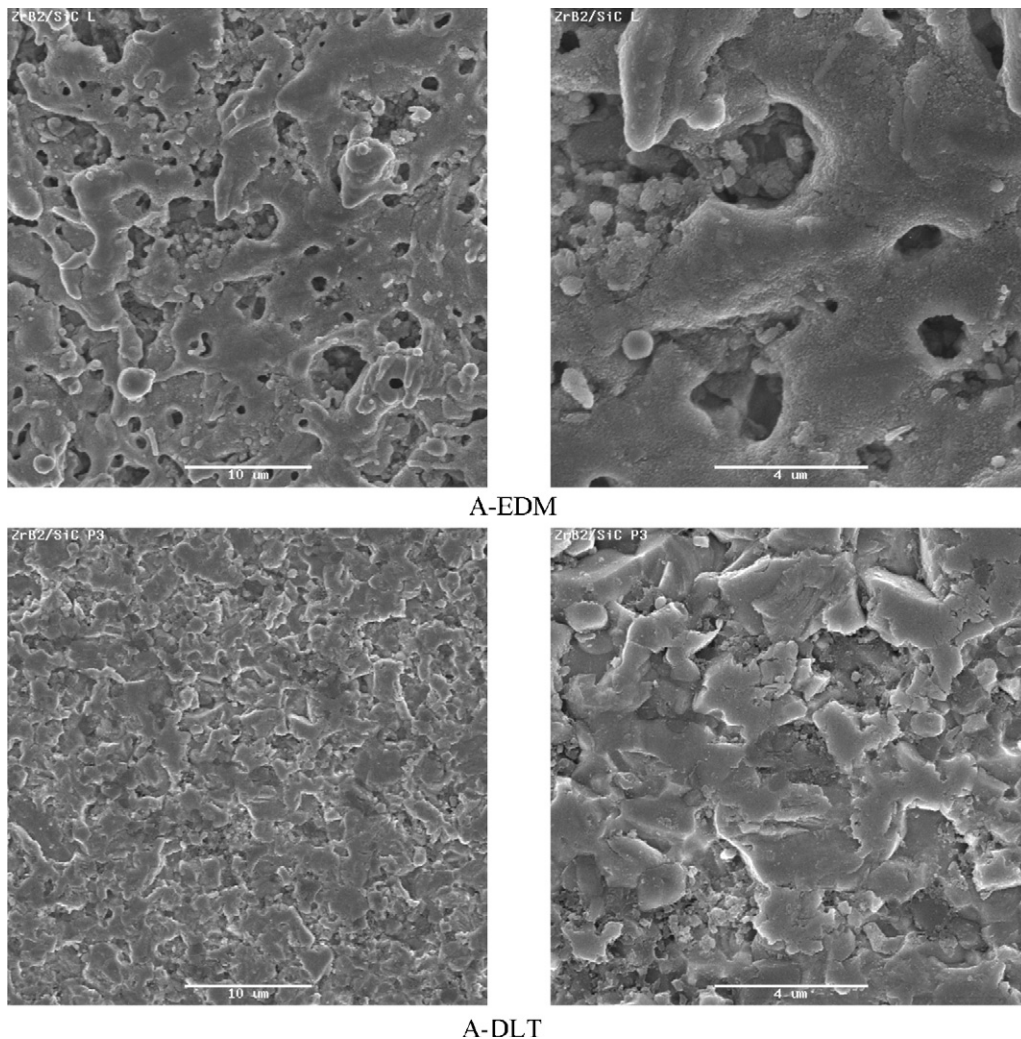
Fig. 1. SEM micrographs of (a), (b) EDMed, and (c), (d) DLTed pristine ZrB$_2$–SiC (material A) samples.

B-EDM

B-DLT
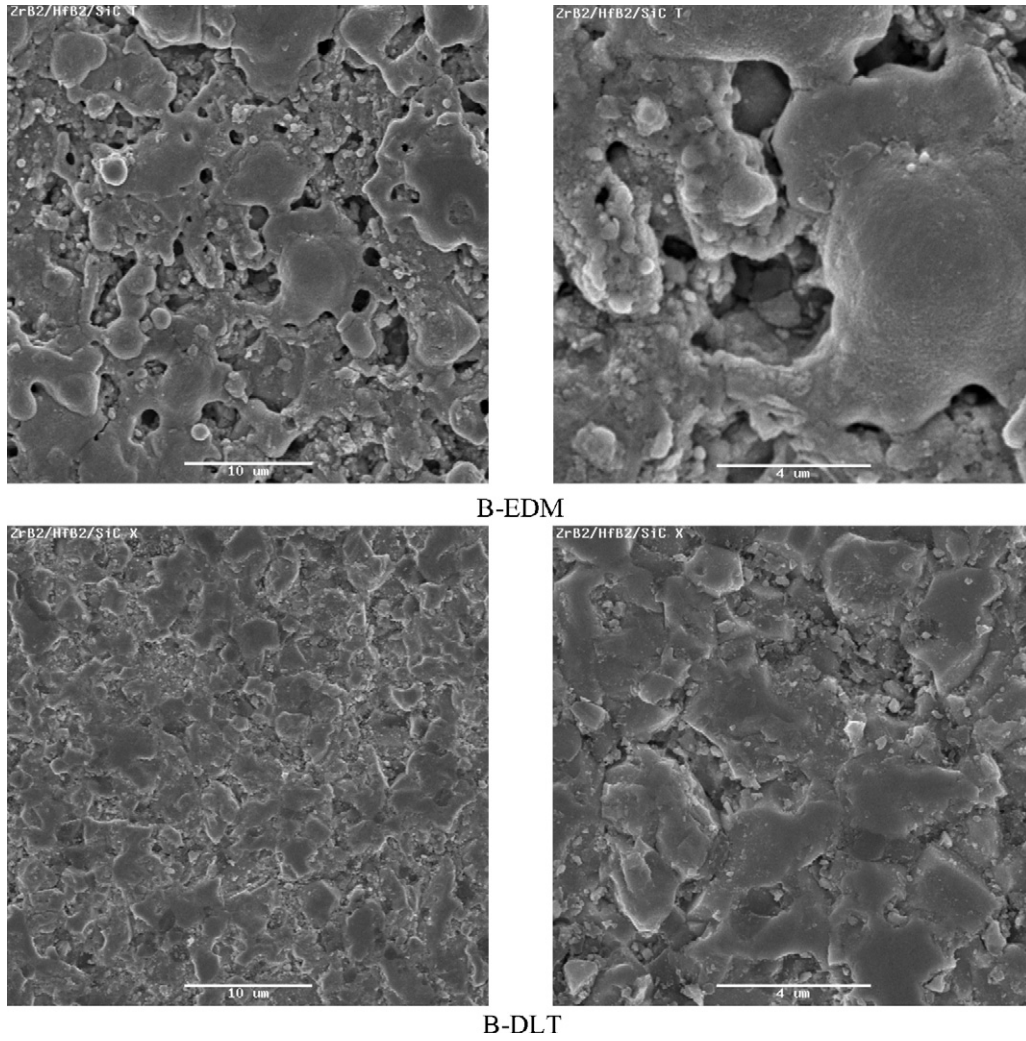
Fig. 2. SEM micrographs of the (a), (b) EDMed, and (c), (d) DLTed pristine ZrB_2–HfB_2–SiC (material B) samples.

X-ray photoelectron spectroscopy (XPS) analyses were performed on a SIA Riber Cameca UHV device operating at a pressure of 10^{-6} Pa and Al-Kα X-ray beam. The kinetic energy of the photoelectrons was measured using a

Riber Cameca MAC 2 spectroscopic two stage spectrometer.

The analyzer resolution was fixed at 1 eV. Spectrometer energy calibration was made using the Au $4f_{7/2}$ (83.9 ± 0.1 eV)
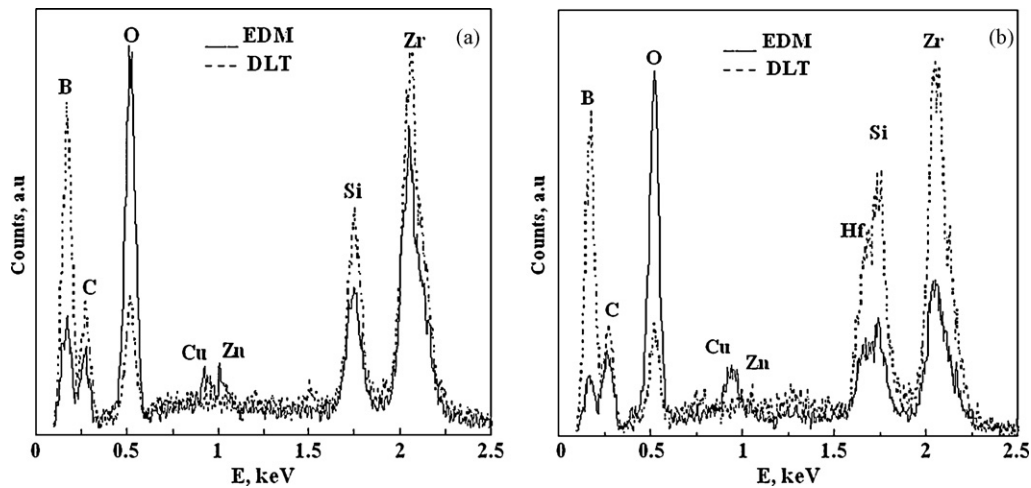
Fig. 3. EDS analysis of the (a) A-EDM and A-DLT pristine samples, (b) B-EDM and B-DLT pristine samples.
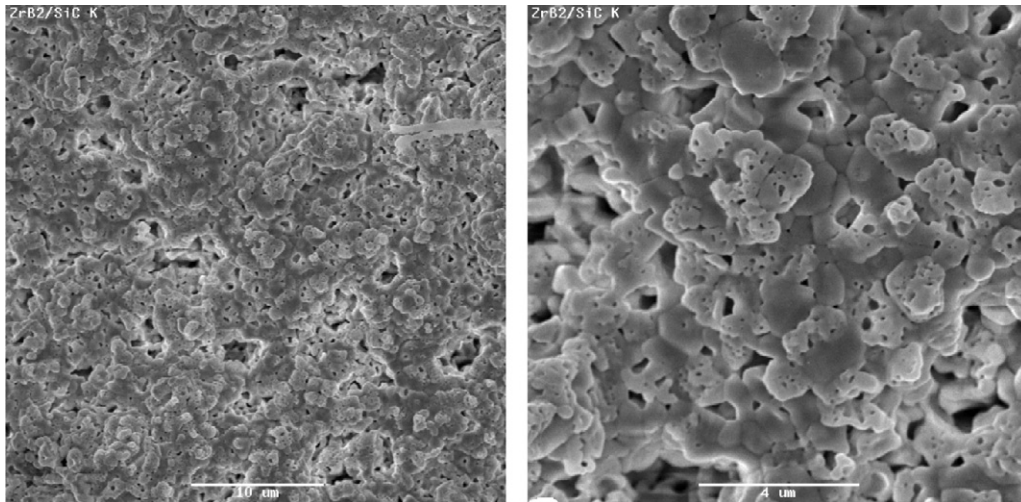
Fig. 4. SEM micrographs of EDM ZrB_2–SiC (material A) tested sample.

and Cu $2p_{3/2}$ (932.8 ± 0.1 eV) photoelectron lines. XPS spectra were recorded in the direct mode (kinetic energy). The Zr $3d_{3/2,5/2}$, Si $2p_{1/2,3/2}$, Hf $4f_{5/2,7/2}$, O 1s, B 1s and C 1s photoelectron lines were examined. Due to possible electrostatic charging effects, particularly for the samples coated with silica layers, the C 1s line due to carbon present on the surface, which is generally reported at 285 eV, was used to adjust the binding energies of the photoelectron peaks.
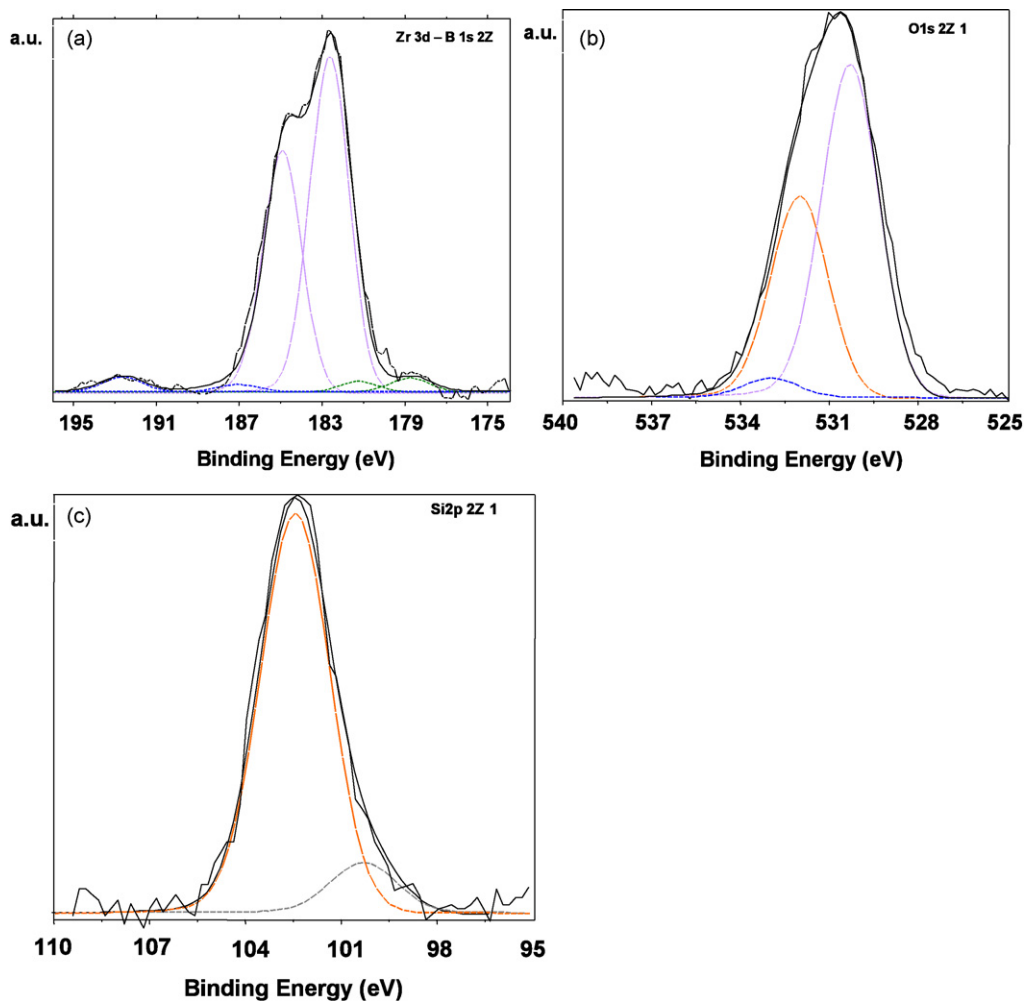
Fig. 5. (a) Zr $3d_{3/2,5/2}$, (b) O 1s, and (c) Si 2p XPS photoelectron peaks for the pristine A-EDM sample.

Based on observations of material surface degradation, by electrons and ions, the ionic sputtering of the film surfaces was made by Ar$^+$ ion beam accelerated under 0.6 keV in order to eliminate the contamination species. The background signal was removed using the Shirley method.[20] The surface atomic concentrations were determined from photoelectron peak areas using the atomic sensitivity factors reported by Scofield[21] or using atomic sensitivity factors determined from reference samples and taking account the transmission function of the analyzer.

3. Results and discussion

By comparing the SEM micrographs of Figs. 1 and 2, the different surface structures between pristine EDMed and DLTed specimens are evident. Samples with different chemical compositions, but obtained by the same machining process, had a similar surface morphology. In particular, EDMed specimens were characterized by a rougher and more irregular surface with respect to DLTed specimens. Surface roughness values were reported in a previous paper.[14]

The EDS spectra of pristine EDMed and DLTed samples are shown in Fig. 3. The surfaces of EDMed materials contained oxygen that further analysis by XPS showed to be bonded to Zr, Hf, Si, and B to form zirconia, hafnia, silica, and boria, respectively. The reaction products of diboride-based composites were due to the EDM machining, which was also responsible for the contamination of metallic copper and zinc.[22]

3.1. Material A

Post-test optical inspection of the surface of sample A-EDM, after it reached its highest temperature of about 1750 °C, revealed a rough layer in the central region where the measurements of the temperature and of the recombination were performed (Fig. 4). EDS analyses performed on that region revealed that this rough surface contained only zirconium and oxygen.

The morphology and chemical composition of the surface of the A-EDM sample after testing (mainly zirconia) can be explained by the temperature level reached during
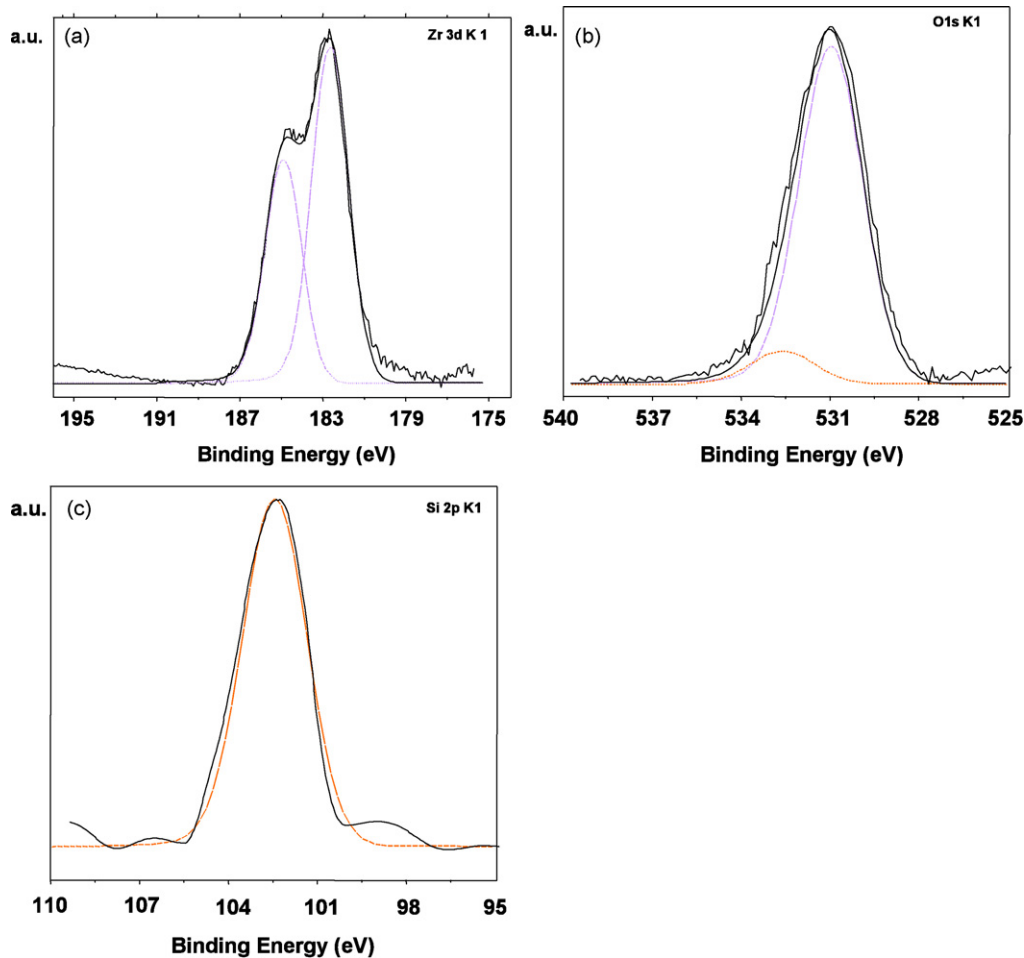

Fig. 6. (a) Zr 3d$_{3/2,5/2}$, (b) O 1s, and (c) Si 2p XPS photoelectron peaks for the tested A-EDM sample at 1750 °C.

Table 4

Main positions (±0.1 eV) and atomic compositions (%) measured from O 1s, C 1s, B 1s, Zr 3d$_{3/2,5/2}$, Si 2p$_{1/2,3/2}$ and Hf 4f$_{5/2,7/2}$ photoelectron peaks collected for A-EDM, tested A-EDM (1750 °C), B-DLT and tested B-DLT (1550 °C) samples.

Sample	Main positions of photoelectron peaks (±0.1 eV) and measured atomic compositions (%)											
	O 1s		C 1s		B 1s		Zr 3d$_{3/2,5/2}$		Si 2p$_{1/2,3/2}$		Hf 4f$_{5/2,7/2}$	
A-EDM	530.7	53.2	285.0	21.4	192.8	3.5	182.8	12.9	103.1	9.0	–	–
Tested A-EDM (1750 °C)	530.8	59.2	285.0	13.2	–	–	183.0	25.3	103.2	2.3	–	–
B-DLT	531.4	38.4	285.0	23.0	192.8	15.7	178.5	15.9	100.6	5.4	14.5	1.5
Tested B-DLT (1550 °C)	532.3	64.3	285.0	1.7	192.8	2.2	183.0	2.9	103.2	28.7	14.6	0.2

the catalycity test. The volatilization and/or the active oxidation of SiC resulted in the absence of silica, considering that the maximum temperature recorded during the catalycity test was about 1750 °C. The presence of a dense and smooth borosilicate vitreous layer has been already detected on the same material that was only tested up to 1550 °C,[14,18] in accordance with the passive oxidation process expected for SiC.[23–25]

XPS spectra of the pristine sample and of material A-EDM tested at 1750 °C, shown in Figs. 5 and 6, confirmed the presence of a zirconia layer, which was due to the volatilization of silica after the highest temperature treatment. The Zr 3d and O 1s photoelectron peaks of the pristine sample were fitted, respectively, into two main components with binding energies of 182.8 ± 0.1 eV (Zr 3d$_{5/2}$) and 185.1 ± 0.1 eV (Zr 3d$_{3/2}$) for the Zr–O contribution and at 530.4 eV for the O–Zr bond and 532.2 eV for the O–Si bond (Fig. 5). The presence of an oxide layer on the pristine A-EDM sample is due to the finishing treatment as already explained. The ED machining leads to the presence of zirconia and some silica on the pristine sample. For the sample tested at 1750 °C, the Zr 3d photoelectron peaks were fitted to the curves related to Zr–O binding energies (Fig. 6). For the O 1s photoelectron peak, the main component peak located at 530.8 ± 0.1 eV (Fig. 6) is characteristic of the presence of O–Zr environments in a zirconia compound.

Fig. 6 also shows the Si 2p$_{1/2,3/2}$ photoelectron peak collected for sample A-EDM tested at 1750 °C. Only one component was detected at 103.2 ± 0.1 eV attributed to Si–O bonds in the SiO$_2$ compound.

Similar results and conclusions can be drawn by analyzing SEM images and EDS spectra for the tested A-DLT sample: no significant difference in surface morphology were observed for the same composition machined by different methods after plasma exposure, and in both cases the mass loss was about 0.30%. Tables 4 and 5 report the main component positions, nature of the chemical bonds and atomic compositions measured from O 1s, C 1s, B 1s, Zr 3d$_{3/2,5/2}$, Si 2p$_{1/2,3/2}$ and Hf 4f$_{5/2,7/2}$ photoelectron peaks collected for A-EDM, tested A-EDM (1750 °C), B-DLT and tested B-DLT (1550 °C) samples. From these results, tested A-EDM is mainly composed of zirconia (25.3%) and some silica (2.3%).

The differences between the catalytic behavior of the A-EDM material with respect to A-DLT have, therefore, to be explained considering the different starting surface composition and morphology due to the machining method. In particular, the presence of silica (7.7%) on the surface of the pristine A-EDM material (Table 5) from the start of the test may account for the lower recombination coefficient values exhibited by this sample.[15,26–32]

Table 5

Components positions (±0.1 eV), nature and rate (%) of main chemical bonds measured from deconvoluted photoelectron peaks (O 1s, B 1s, Zr 3d$_{3/2,5/2}$ and Si 2p$_{1/2,3/2}$) collected for A-EDM, tested A-EDM (1750 °C), B-DLT and tested B-DLT (1550 °C) samples.

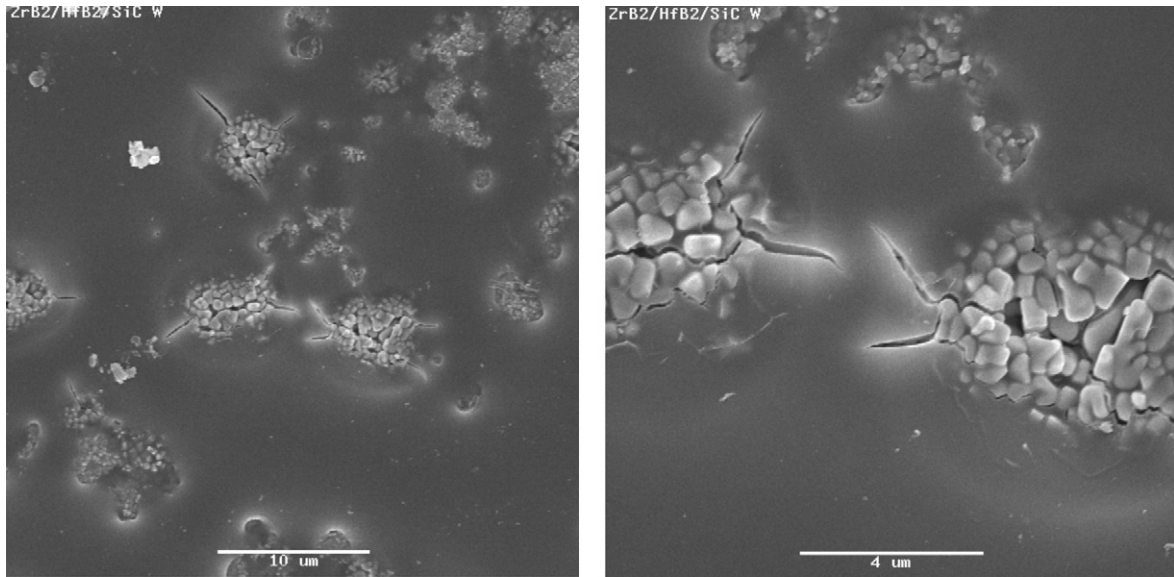| Sample	Components positions (±0.1 eV), percentage and nature of main chemical bonds										
	O 1s			B 1s		Zr 3d$_{3/2,5/2}$				Si 2p$_{1/2,3/2}$	
						Zr 3d$_{3/2}$	Zr 3d$_{5/2}$	Zr 3d$_{3/2}$	Zr 3d$_{5/2}$		
A-EDM	533.2	532.1	530.8	192.8	187.5	185.0	182.8	181.2	178.7	103.2	100.6
	1.8	20.4	31.0	2.4	1.1	12.4		0.5		7.7	1.3
	O-B	O-Si	O-Zr	B-O	B-Zr	Zr-O		Zr-B		Si-O	Si-C
Tested A-EDM (1750 °C)	–	532.2	530.8		–	185.1	182.9	–		103.2	
		4.2	55.0			25.3				2.3	
		O-Si	O-Zr			Zr-O				Si-O	
B-DLT	533.2	532.2	530.8	192.8	187.5	185.0	182.9	181.2	178.7	103.2	100.6
	10.0	13.4	15.0	9.5	6.2	6.9		9.0		1.6	3.8
	O-B	O-C	O-Zr	B-O	B-Zr	Zr-O		Zr-B		Si-O	Si-C
Tested B-DLT (1550 °C)	–	532.3	530.8	192.8		185.1	182.9	–		103.2	–
		59.9	4.4	10.5	–					28.7	
		O-Si	O-Zr	B-O		Zr-O				Si-O	

Fig. 7. SEM micrographs of DLT ZrB_2–HfB_2–SiC (material B) tested sample.

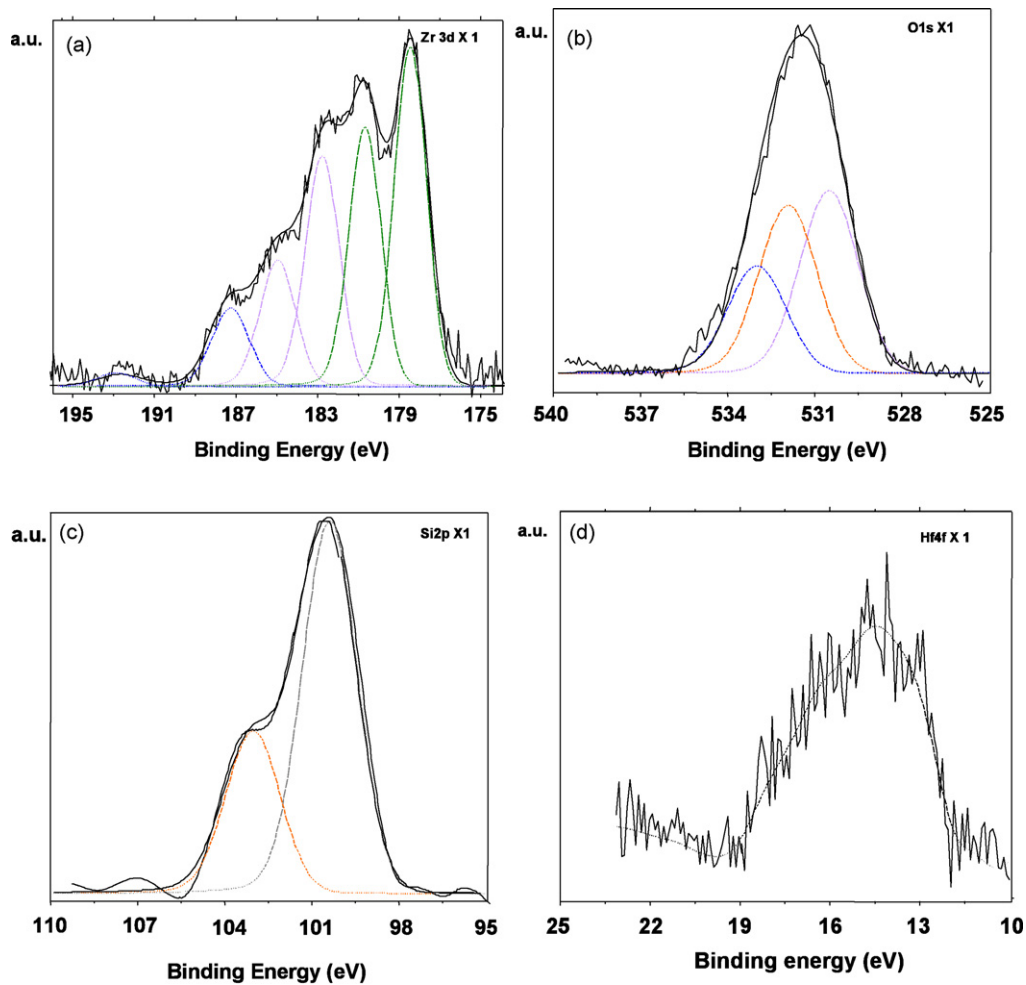Fig. 8. (a) Zr $3d_{3/2,5/2}$, (b) O 1s, (c) Si 2p, and (d) Hf $4f_{5/2,7/2}$ XPS photoelectron peaks for the pristine B-DLT sample.
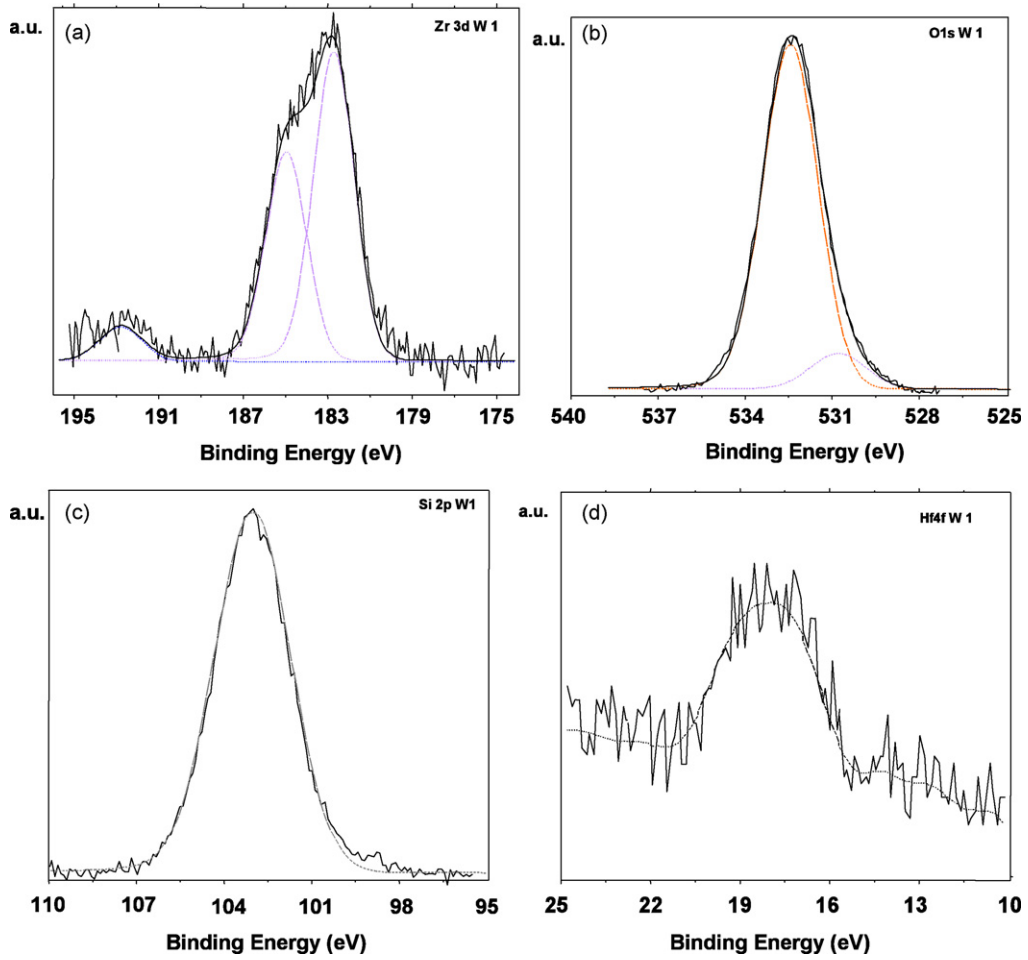
Fig. 9. (a) Zr 3d$_{3/2,5/2}$, (b) O 1s, (c) Si 2p, and (d) Hf 4f$_{5/2,7/2}$ XPS photoelectron peaks for the tested B-DLT sample at 1550 °C.
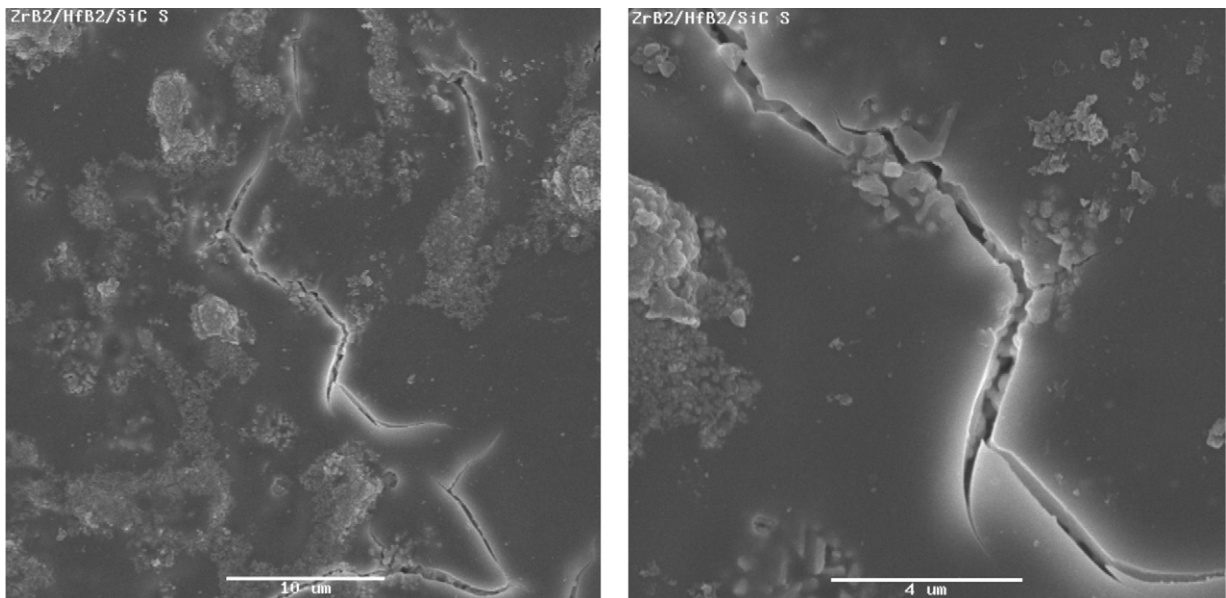

Fig. 10. SEM micrographs of EDM ZrB$_2$-HfB$_2$-SiC (material B) tested sample at 1550 °C.

3.2. Material B

After testing, B-DLT had a surface morphology similar to tested A-EDM at 1550 °C[14,18] and A-DLT (Fig. 7). The maximum temperature during testing was about 1550 °C. EDS analyses revealed that the central region contained silicon, hafnium, zirconium, and oxygen.

XPS spectra, shown in Figs. 8 and 9, indicated the presence of Zr–O and Zr–B bonds in ZrO_2 and ZrB_2 compounds, respectively, as well as Si–O bonds in SiO_2 compound, on the surface of material B after testing. The XPS spectra of the pristine sample (Fig. 8) had several fitted peaks relative to Zr–B bonds at 178.7 ± 0.1 eV (Zr $3d_{5/2}$) and at 181.2 ± 0.1 eV (Zr $3d_{3/2}$), Zr–O bonds at 182.9 ± 0.1 eV (Zr $3d_{5/2}$) and at 185.0 ± 0.1 eV (Zr $3d_{3/2}$), B–Zr bonds at 187.5 ± 0.1 eV (B 1s) and B–O bonds at 192.8 ± 0.1 eV (B 1s) corresponding to the presence of ZrB_2 and some ZrO_2 on the surface along with a small amount of B_2O_3 (9.5%, B–O bond). The O 1s photoelectron peaks of the pristine sample were fitted respectively in three components at binding energies of 530.4 ± 0.1 eV (O–Zr bond), 532.2 ± 0.1 eV (O–C + O–Si bonds) and 533.2 ± 0.1 eV (O–B bond). Fig. 8 also shows the results of the peak fitting procedure Si $2p_{1/2,3/2}$ photoelectron peak. The main component located at 100.6 ± 0.1 eV is attributed to Si–C bonds (SiC compound). The component detected at 103.2 ± 0.1 eV is attributed to Si–O bonds (SiO_2 compounds). The main Hf $4f_{7/2}$ photoelectron peak and the Hf $4f_{5/2}$ shoulder were detected at about 14.5 ± 0.1 and 16.3 ± 0.1 eV respectively (Hf–B bonds).[33]

In tested B-DLT, the main compound detected was silica (28.7%, Si–O bond at 103.2 ± 0.1 eV), followed by boria (10.5%, B–O bonds) and zirconia (3–4%, O–Zr bond at 530.8 ± 0.1 eV). From Fig. 9, the weak Hf $4f_{5/2,7/2}$ photoelectron peak detected at about 18.0 ± 0.1 eV could be attributed to Hf–O bonds in hafnia (about 0.2%).[34,35] The peak temperature of 1550 °C reached during the catalycity test resulted in the presence of silica along with hafnia and zirconia. At this temperature, the silica is stable on the sample surface and only a small mass loss of about 0.25% was observed.

In the case of A-EDM, the peak temperature of 1750 °C reached during the test was above the thermodynamic stability limit of silica. Tested B-EDM (Fig. 10) had a uniform surface characterized by the same morphology already observed for the central region of tested B-DLT (Fig. 7). It also consisted of basically the same chemical composition described before for the central region of tested B-DLT.

Material B samples machined by EDM and DLT showed similar catalytic behavior with no significant differences through the entire range of temperatures investigated. Pristine B-EDM samples showed different surface composition and morphology compared to B-DLT (similar to the pristine A-EDM and A-DLT samples) due to the effect of EDM machining, yet in this case this difference did not seem to affect the catalytic behavior. Since EDS analysis did not allow for a quantitative assessment of the amount of silica on the surface of the pristine EDMed samples, it can be hypothesized that in the case of the B composition, the higher refractoriness associated with the presence of HfB_2 may have limited the surface modification due to machining,

consequently reducing the effect of these modifications on the catalytic behavior.

Composition B had a higher recombination coefficient than material A across the temperature range investigated (see Tables 2 and 3). The differences in the values of the recombination coefficient were corroborated by the differences in the surface morphology and composition exhibited by the two materials prior to, and after, plasma exposure.

4. Conclusions

In-depth microstructural investigation by SEM, EDS, and XPS analyses performed in this study have shown that the evolution of the recombination coefficient with temperature in atmospheric reentry conditions is sensitive to surface composition and morphology in UHTCs.

The two UHTC compositions analyzed, characterized by a common UHTC base matrix based upon ZrB_2–SiC, have shown different surface modification after high temperature plasma exposure relative to the maximum temperature reached. For temperatures lower than 1550 °C, mainly silica was present on the surface of the post-test material. When higher temperatures were reached, close to 1750 °C, only zirconia was detected on the surface due to the high volatilization rate of silica and boria.

Finally, these samples had low catalytic activity (about 10^{-2}) when a borosilicate glassy layer with some zirconia was formed on the surface below 1550 °C. When zirconia was present in higher concentrations, the recombination coefficient increased to about 0.1. Moreover, the presence of HfB_2 in material B led to higher recombination coefficients, probably due to the higher catalycity of hafnia compared to zirconia.

This study highlighted the extreme complexity of UHTC oxidation behavior, as well as the need for an exhaustive knowledge of the phenomena regulating surface oxidation in order to explain the surface properties of this class of materials.

References

1. Fahrenholtz WG, Hilmas GE, Talmy IG, Zaykoski JA. Refractory diborides of zirconium and hafnium. *J Am Ceram Soc* 2007;**90**:1347–64.
2. Mroz C. Zirconium diboride. *Am Ceram Soc Bull* 1994;**73**:141–2.
3. Upadhya K, Yang J-M, Hoffman WP. Materials for ultra-high temperature structural applications. *Am Ceram Soc Bull* 1997;**58**:51–6.
4. Gasch M, Ellerby D, Irby E, Beckman S, Gusman M, Johnson S. Processing, properties and arc-jet oxidation of hafnium boride/silicon carbide ultra high temperature ceramics. *J Mater Sci* 2004;**39**:5925–37.
5. Wang C, Yang J-M, Hoffman WP. Thermal stability of refractory carbide/boride composites. *Mater Chem Phys* 2002;**74**:272–81.
6. Naslain R. *High temperature ceramic matrix composites*. Bordeaux: Woodhead Publications; 1993. pp. 215–229.
7. Laux T, Ullmann T, Auweter-Kurtz M, Hald H, Kurz A. Investigation of thermal protection materials along an X-38 re-entry trajectory by plasma wind tunnel simulations. In: *Proceeding of the 2nd international symposium on atmospheric reentry vehicles and systems*. 2001. p. 1–9.
8. Naslain R, Lamalle J, Zulian JL. *Composite materials for high temperature applications*. Paris: AMAC; 1990. pp. 315–325.
9. Messiah A. *Developments in the science and technology of composite materials*. London: Elsevier; 1989. pp. 99–110.

10. Mühlratzer A, Leuchs M. Applications of non-oxide CMCs. In: *Proceedings of the 4th international conference on high temperature ceramic matrix composites*. 2001. p. 288–98.

11. Monteverde F, Bellosi A, Guicciardi S. Processing and properties of zirconium diboride-based composites. *J Eur Ceram Soc* 2002;**22**:279–88.

12. Monteverde F, Bellosi A, Scatteia L. Processing and properties of ultra high temperature ceramics for space applications. *Mater Sci Eng A* 2008;**485**:415–21.

13. Nakamura M, Shigematsu I, Kanayama K, Hirai Y. Surface damage in ZrB_2-based composite ceramics induced by electro-discharge machining. *J Mater Sci* 1991;**26**:6078–82.

14. Scatteia L, Alfano D, Monteverde F, Sans J-L, Balat-Pichelin M. Effect of the machining method on the catalycity and emissivity of ZrB_2 and ZrB_2–HfB_2-based ceramics. *J Am Ceram Soc* 2008;**91**:1461–8.

15. Balat-Pichelin M, Badie JM, Berjoan R, Boubert P. Recombination coefficient of atomic oxygen on ceramic materials under earth re-entry conditions by optical emission spectroscopy. *Chem Phys* 2003;**291**:181–94.

16. Balat-Pichelin M, Bedra L, Gerasimova O, Boubert P. Recombination of atomic oxygen on α-Al_2O_3 at high temperature under air microwave-induced plasma. *Chem Phys* 2007;**340**:217–26.

17. Balat M, Czerniak M, Badie JM. Thermal and chemical approaches for oxygen catalytic recombination evaluation on ceramic materials at high temperature. *Appl Surf Sci* 1997;**120**:225–38.

18. Scatteia L, Borrelli R, Cosentino G, Bêche E, Sans J-L, Balat-Pichelin M. Catalytic and radiative behaviors of ZrB_2–SiC ultrahigh temperature ceramic composites. *J Spacecraft Rockets* 2006;**43**:1004–12.

19. Balat-Pichelin M, Vesel A. Neutral oxygen atom density in the MESOX air plasma solar furnace facility. *Chem Phys* 2006;**327**(1):112–8.

20. Shirley DA. High-resolution X-ray photoemission spectrum of the valence bands of gold. *Phys Rev B* 1972;**5**:4709–14.

21. Scofield JH. Hartree-Slater subshell photoionization cross-sections at 1254 and 1487 eV. *J Electron Spectrosc & Related Phenom* 1976;**8**:129–37.

22. Khanra AK, Pathak LC, Godkhindi MM. Microanalysis of debris formed during electrical discharge machining (EDM). *J Mater Sci* 2007;**42**: 872–7.

23. Balat MJH. Determination of the active-to-passive transition in the oxidation of silicon carbide in standard and microwave-excited air. *J Eur Ceram Soc* 1996;**16**:55–62.

24. Eck J, Balat-Pichelin M, Charpentier L, Bêche E, Audubert F. Behavior of SiC at high temperature under helium with low oxygen partial pressure. *J Eur Ceram Soc* 2008;**28**:2995–3004.

25. Chamberlain A, Fahrenoltz WG, Hilmas GE, Ellerby D. Oxidation of ZrB_2–SiC ceramics under atmospheric and reentry conditions. *Refr Appl Trans* 2005;**1**:1–8.

26. Marschall J, Chamberlain A, Crunkleton D, Rogers B. Catalytic atom recombination on ZrB_2/SiC and HfB_2/SiC ultrahigh-temperature ceramic composites. *J Spacecraft Rockets* 2004;**41**:576–81.

27. Balat M, Czerniak M, Badie JM. Ceramic catalysis evaluation at high temperature using thermal and chemical approaches. *J Spacecraft Rockets* 1999;**36**:273–9.

28. Steward WA, Jumper EJ. Model for oxygen recombination on silicon dioxide surfaces. *J Thermophys Heat Transfer* 1991;**5**:284–91.

29. Carleton KL, Marinelli WJ. Spacecraft thermal energy accommodation from atomic recombination. *J Thermophys Heat Transfer* 1992;**6**:650–5.

30. Willey J. Spacecraft thermal energy accommodation from atomic recombination. *J Thermophys Heat Transfer* 1993;**7**:55–62.

31. Jumper EJ, Seward WA. Model for oxygen recombination on reaction-cured glass. *J Thermophys Heat Transfer* 1994;**8**:460–5.

32. Cartry G, Magna L, Cernogora G. Atomic oxygen recombination on fused silica: modelling and comparison to low-temperature experiments (300 K). *J Phys D: Appl Phys* 2000;**33**:1303–4.

33. Perkins CL, Singh R, Tanaka T, Trenary M. Characterization of hafnium diboride HfB_2 (0001) by XPS. *Surf Sci Spectra* 2000;**7**:316–21.

34. Maida, O., Fukayama, K. I., Takahashi, M. and Kobayashi, H., Interface states for HfO_2/Si structure observed by X-ray photoelectron spectroscopy measurements under bias. *Appl. Phys. Lett.*, 2007, **101**, 034108-1r-r034108-7.

35. Tanner, C. M., Choi, J. and Chang, J., Electronic structure and band alignment at the HfO_2/4H-SiC interface. *Appl. Phys. Lett.*, 2006, **89**, 122112-1r-r122112-3.